Large-scale electronic structure theory for simulating nanostructure processes

Large-scale electronic structure theory for simulating nanostructure processes

T Hoshi and T Fujiwara

Department of Applied Physics, University of Tokyo, 7-3-1 Hongo, Bunkyo-ku, Tokyo 113-8656, Japan
and
Core Research for Evolutional Science and Technology (CREST-JST), Japan Science and Technology Agency, 4-1-8 Honcho, Kawaguchi-shi, Saitama 332-0012, Japan

Abstract

Fundamental theories and practical methods for large-scale electronic structure calculations are given, in which the computational cost is proportional to the system size. Accuracy controlling methods for microscopic freedoms are focused on two practical solver methods, the Krylov-subspace method and the generalized-Wannier-state method. A general theory called the 'multi-solver' scheme is also formulated, as a hybrid between different solver methods. Practical examples are carried out in several insulating and metallic systems with 10^3–10^5 atoms. All the theories provide general guiding principles of constructing an optimal calculation for simulating nanostructure processes, since a nanostructured system consists of several competitive regions, such as bulk and surface regions, and the simulation is designed to reproduce the competition with an optimal computational cost.

1. Introduction

Electronic structure theory plays a crucial role in understanding and controlling nanostructures, structures in nanometre and ten-nanometre scales. Dynamical simulation in these scales is, however, impractical for the present standard methodology, such as the Car–Parrinello method [1], owing to its heavy computational cost. Since the 1990s, many calculation methods and related techniques have been proposed for large systems, systems with thousands of atoms or more, by calculating the one-body density matrix or the Green's function, instead of one-electron eigenstates [2–19]. In these methodologies, calculation is carried out with the real-space representation and a physical quantity $\langle X \rangle$ is given as a trace form

$$\langle X \rangle = \text{Tr}[\rho X] = \int \int \mathrm{d}\boldsymbol{r}\, \mathrm{d}\boldsymbol{r}'\, \rho(\boldsymbol{r}, \boldsymbol{r}') X(\boldsymbol{r}', \boldsymbol{r}). \tag{1}$$

Here the one-body density matrix ρ is defined, from occupied one-electron eigenstates $\phi_k(\boldsymbol{r})$, as
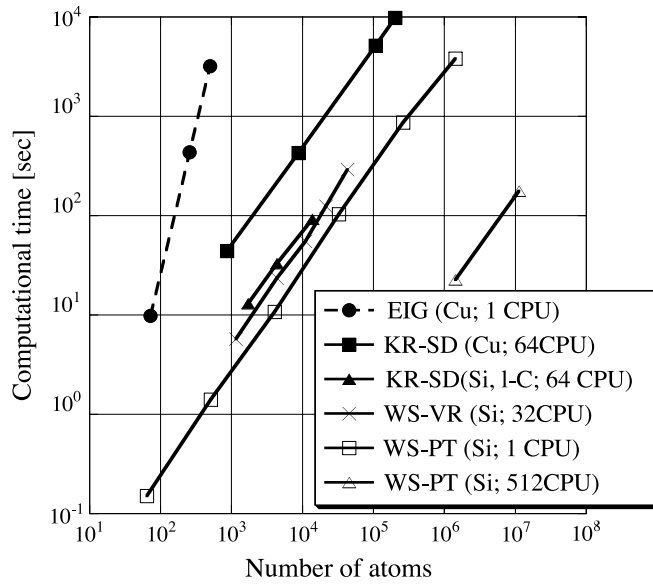
Figure 1. The computational time as a function of the number of atoms (N) ([15, 17], this work). Several metallic (fcc Cu and liquid C) and insulating (bulk Si) systems are calculated up to 11 315 021 atoms. The time was measured for the electronic structure calculation with a given atomic structure. The calculations were carried out by the conventional eigenstate calculation (EIG) and by our methods for large systems: (i) Krylov-subspace method with subspace-diagonalization procedure (KR-SD), (ii) Wannier-state method with variational procedure (WS-VR) and (iii) Wannier-state method with perturbative procedure (WS-PT). For '1CPU' computations, we used a single Pentium 4^{TM} processor at 2 GHz. Parallel computations were carried out by an SGI Origin 3800^{TM} (for the WS-PT method), an Origin 2800^{TM} (for the WS-VR method) and an Altix 3700^{TM} (for the KR-SD method). See the text for details.

$$\rho \equiv \sum_{k}^{occ} |\phi_k^{(eig)}\rangle \langle \phi_k^{(eig)}|. \tag{2}$$

One can find that, if the matrix $X(r, r')$ is of short range, the off-diagonal long-range component of the density matrix does not contribute to the physical quantity $\langle X \rangle$, which is important for the practical success of large-scale calculations [2]. Actual calculation methods and their applications are found in recent reviews [3, 4] or papers [5–19]. A set of theories and program codes have been developed in our group and a test calculation of figure 1 shows that the computational cost is 'order N' or proportional to the system size (N) for the calculations with 10^3–10^7 atoms [15, 17, 16, 20, 19].

A practical success in an application study always requires balance between the accuracy and the computational cost. Every calculation method has several controlling parameters and one should establish a systematic way of setting them in optimal values. Here we remember that a nanostructure is composed of several comparable regions with essential difference in electronic structure, such as bulk and surface regions. Since the competition of these regions gives various structural and functional properties of nanostructures, the requirement on dynamical simulation of a nanostructure is to reproduce the competition, or to reproduce the difference in electronic structure among the regions, throughout the process.

In this paper, we will show how to construct an optimal calculation scheme for nanostructure processes. The essential concepts are (i) the method of controlling the accuracy and the computational cost by monitoring residuals for microscopic or basis freedoms and

(ii) choice or combination of different calculation methods. Hereafter the phrase 'solver method' is used for a practical calculation method of density matrix ρ with a given Hamiltonian H.

This paper is organized as follows: in section 2, we will explain the foundation of two methods, the Krylov-subspace method and the generalized-Wannier-state method. They are practical solver methods to calculate the density matrix for a given system and we will compare them, in section 2.3, from a practical viewpoint. In section 3, we will construct a methodology of the 'multi-solver' scheme, as a hybrid or combination of different solver methods. Several applications such as molecular dynamics (MD) simulations will be presented in section 4, so as to clarify the methodological points. In the present paper, we limit the formulations to those for a Hamiltonian H as a real-symmetric matrix. Practical calculations were carried out with Hamiltonians in the Slater–Koster (tight-binding) form; the Hamiltonian for fcc Cu is constructed from the first-order form $H^{(1)}$ of the linear muffin-tin orbital theory [21] and those for C and Si are typical ones in [22] and [23], respectively.

2. Theory (1) practical solver methods

2.1. Solver methods with Krylov subspace

The Krylov subspace is a general mathematical concept defined as the linear space of

$$\mathcal{K}_\nu(H, |j\rangle) \equiv \text{span}\left\{|j\rangle,\ H|j\rangle,\ H^2|j\rangle, \ldots, H^{\nu-1}|j\rangle\right\}. \tag{3}$$

Here the 'starting' vector ($|j\rangle$) and the dimension of the subspace (ν) are arbitrary. Many iterative methods, such as the standard conjugate-gradient method, are formulated with the Krylov subspace. See a recent textbook [24], for example. In the present context, the matrix H is a Hamiltonian and $|j\rangle$ is a real-space basis. A large-scale calculation can be realized when the density matrix $\langle i|\rho|j\rangle$ is constructed within the Krylov subspace $\mathcal{K}_\nu(H, |j\rangle)$. The Krylov-subspace method also enables us to calculate the Green's function $\langle i|G|j\rangle$, which gives directly the information on electronic states, such as the density of states (DOS). When the dimension ν is equal to that of the original Hamiltonian matrix H, the linear space of equation (3) is complete and all the calculation results are exact [24].

2.1.1. Subspace-diagonalization method.
Here we explain a practical solver method with the Krylov subspace, called the 'subspace-diagonalization method' (KR-SD) [16]; first, we construct an orthogonal basis set $\{|K_n^{(j)}\rangle\}$ for the Krylov subspace ($\langle K_n^{(j)}|K_m^{(j)}\rangle = \delta_{nm}$),

$$\mathcal{K}_\nu(H, |j\rangle) = \text{span}\{|K_1^{(j)}\rangle \equiv |j\rangle, |K_2^{(j)}\rangle, \ldots, |K_\nu^{(j)}\rangle\} \tag{4}$$

by the Lanczos procedure, a three-term recurrence formula. The nth basis $|K_n^{(j)}\rangle$ is constructed in the n-dimensional Krylov subspace ($|K_n^{(j)}\rangle \in \mathcal{K}_n(H, |j\rangle)$). As a result, a reduced Hamiltonian matrix

$$\left(H^{K(j)}\right)_{nm} \equiv \langle K_n^{(j)}|H^{(j)}|K_m^{(j)}\rangle \tag{5}$$

is obtained as an explicit ($\nu \times \nu$) matrix. A typical subspace dimension is $\nu = 30$ in MD simulations. Then, we diagonalize the reduced (small) matrix

$$H^{K(j)}|v_\alpha^{(j)}\rangle = \varepsilon_\alpha^{(j)}|v_\alpha^{(j)}\rangle, \tag{6}$$

with a negligible computational cost. The resultant eigenvectors $|v_\alpha^{(j)}\rangle$ are described as the set of coefficients $C_{\alpha m}^{(j)} \equiv \langle K_m^{(j)}|v_\alpha^{(j)}\rangle$.

The density matrix is obtained by

$$\langle i|\rho|j\rangle \Rightarrow \langle i|\rho^{K(j)}|j\rangle \tag{7}$$

$$= \sum_n^\nu \langle i|K_n^{(j)}\rangle\langle K_n^{(j)}|\rho^{K(j)}|j\rangle, \tag{8}$$

with the definition of

$$\rho^{K(j)} \equiv \sum_\alpha |v_\alpha^{(j)}\rangle f_\tau(\varepsilon_\alpha^{(j)} - \mu)\langle v_\alpha^{(j)}|. \tag{9}$$

Here the occupation number $f_\tau(\varepsilon - \mu)$ is given by the Fermi–Dirac function with a temperature (level-broadening) parameter τ and the chemical potential μ. The chemical potential is determined by the bisection method. The Green's function $\langle i|G(z)|j\rangle$ can be calculated in a similar manner [16]. In short, the present procedure is a standard quantum mechanical calculation for eigenstates, except for the point that the calculation is carried out within the Krylov subspace. Therefore, it is straightforward to apply the method to calculations with a nonorthogonal basis set, in which a generalized eigenvalue equation, instead of equation (6), is solved within the subspace.

2.1.2. Shifted conjugate-orthogonal conjugate-gradient method. Another solver method with the Krylov subspace was formulated and called the 'shifted conjugate-orthogonal conjugate-gradient' (SCOCG) method [19]. Its foundation is given by a mathematical theorem proved recently [25]. The practical procedure is based on an iterative solver method for the linear equation of the Green's function,

$$(z - H)|x_j\rangle = |j\rangle, \tag{10}$$

because $G_{ij} = \langle i|x_j\rangle = \langle i|(z - H)^{-1}|j\rangle$. The density matrix is obtained by

$$\rho_{ij} = -\frac{1}{\pi} \int_{-\infty}^\infty \text{Im}\, G_{ij}(\varepsilon + \text{i}0) f_\tau(\varepsilon - \mu)\, \text{d}\varepsilon. \tag{11}$$

The SCOCG method and KR-SD method share many common features but are different in the numerical treatment. See the original paper [19] for detailed comparison. For the present time, we use, mainly, the KR-SD method for MD simulation and we think that the SCOCG method is suitable to discuss a very fine energy spectrum of the Green's function [19].

2.1.3. Accuracy control with residual. So as to monitor the accuracy during the simulation, we calculate a residual vector of the Green's function [19]

$$|\delta G_j\rangle \equiv (z - H)G|j\rangle - |j\rangle. \tag{12}$$

The residual vector is defined individually for the basis suffix j. We observed that the required subspace dimension $\nu = \nu^{(j)}$ for a given criterion on the residual vector is different among surface and bulk regions [19]. Such a determination of the controlling parameters $\{\nu^{(j)}\}$ is an example of the accuracy control for microscopic or basis freedoms.

2.2. Solver methods with generalized Wannier state

Another method for obtaining the density matrix in large systems is formulated using the generalized Wannier state [26, 27, 5, 7, 28, 11, 29, 30]. A physical picture of the generalized Wannier states is a localized chemical wavefunction in condensed matter, such as a bonding orbital or a lone-pair orbital with a slight spatial extension or 'tail' [5, 7, 28, 11, 29, 30]. Their

wavefunctions $\{\phi_i^{(\mathrm{WS})}\}$ are equivalent to the unitary transformation of occupied eigenstates and satisfy the equation

$$H|\phi_i^{(\mathrm{WS})}\rangle = \sum_{j=1}^{\mathrm{occ}} \varepsilon_{ij}|\phi_j^{(\mathrm{WS})}\rangle, \tag{13}$$

where the matrix ε_{ij} is the Lagrange multipliers for the orthogonality constraint ($\langle\phi_i^{(\mathrm{WS})}|\phi_j^{(\mathrm{WS})}\rangle = \delta_{ij}$). The suffix i of a wavefunction $\phi_i^{(\mathrm{WS})}$ indicates the position of its localization centre, such as a bond site. Since Wannier states give the density matrix ρ in equation (2) by replacing eigenstates $\{\phi_k^{(\mathrm{eig})}\}$ into Wannier states $\{\phi_i^{(\mathrm{WS})}\}$, any physical quantity can be reproduced in the trace form of equation (1).

Our practical solver methods are based on a mapped eigenvalue equation [11, 31] that is equivalent to equation (13),

$$H_{\mathrm{WS}}^{(i)}|\phi_i^{(\mathrm{WS})}\rangle = \varepsilon_{\mathrm{WS}}^{(i)}|\phi_i^{(\mathrm{WS})}\rangle, \tag{14}$$

where

$$H_{\mathrm{WS}}^{(i)} \equiv H + 2\eta_s\bar{\rho}_i - H\bar{\rho}_i - \bar{\rho}_i H \tag{15}$$

$$\bar{\rho}_i \equiv \rho - |\phi_i^{(\mathrm{WS})}\rangle\langle\phi_i^{(\mathrm{WS})}| = \sum_{j(\neq i)}^{\mathrm{occ}} |\phi_j^{(\mathrm{WS})}\rangle\langle\phi_j^{(\mathrm{WS})}|. \tag{16}$$

The energy parameter η_s should be much larger than the highest occupied level. Equation (14) was derived in [11, 31] and will be derived again, from a different theoretical background, in section 3.1 of this paper.

2.2.1. Variational procedure in Wannier-state method. Equation (14) gives a practical iterative procedure to generate Wannier states under explicit localized constraint [11, 15, 17, 31], which is called the variational Wannier state method. See papers [11, 31] for details. The residual vector for each wavefunction $|\phi_i^{(\mathrm{WS})}\rangle$

$$|\delta\phi_i^{(\mathrm{WS})}\rangle \equiv H_{\mathrm{WS}}^{(i)}|\phi_i^{(\mathrm{WS})}\rangle - \varepsilon_{\mathrm{WS}}^{(i)}|\phi_i^{(\mathrm{WS})}\rangle. \tag{17}$$

is monitored for each Wannier state during the simulation, so as to control the accuracy, which realizes the accuracy control for microscopic or basis freedoms, as discussed in the Krylov-subspace method with equation (12). A practical success in the Wannier-state method is realized, when all or a dominant number of wavefunctions are well localized. Examples and technical details are given in section 4.2 and references [11, 15, 31].

2.2.2. Perturbative procedure in Wannier-state method. We developed also a perturbative method [11, 29, 32, 31], in which a perturbation solution of equation (14) is constructed for each Wannier state $|\phi_i^{(\mathrm{WS})}\rangle$,

$$|\phi_i^{(\mathrm{WS})}\rangle \Rightarrow C_i\left(|\phi_i^{(\mathrm{WS})(0)}\rangle + |\phi_i^{(\mathrm{WS})(1)}\rangle\right). \tag{18}$$

Here $|\phi_i^{(\mathrm{WS})(0)}\rangle$ and $|\phi_i^{(\mathrm{WS})(1)}\rangle$ are the unperturbed and first-order perturbation terms, respectively, and the factor C_i is the normalization factor. The unperturbed term $|\phi_i^{(\mathrm{WS})(0)}\rangle$ should be prepared as an input quantity and the perturbation term $|\phi_i^{(\mathrm{WS})(1)}\rangle$ and the normalization factor C_i are determined automatically by the standard first-order perturbation procedure [11, 29, 32, 31]. During a simulation, the weight of the unperturbed term

$$w_0^{(i)} \equiv |\langle\phi_i^{(\mathrm{WS})(0)}|\phi_i^{(\mathrm{WS})}\rangle|^2 \tag{19}$$

is monitored, for each wavefunction, as an accuracy control for microscopic or basis freedoms. In silicon crystal, for example, the ideally sp^3-bonding wavefunction is chosen as the unperturbed term and the weight of the unperturbed term is dominant ($w_0^{(i)} = 0.94$) [11, 29, 31], which validates the perturbative treatment. When the perturbative method is validated, its computational performance is faster than that of the variational method, since the perturbative method gives a simpler procedure to generate the wavefunctions and does not require any iteration loop.

2.3. Comparison between Krylov-subspace and Wannier-state methods

When the Wannier-state methods are compared with the Krylov-subspace methods, the Wannier-state methods require an initial guess of wavefunctions in the variational (iterative) method or an unperturbed term of the wavefunction in the perturbative method. As an example, the reconstruction on the Si(001) surface was calculated with the force on atoms. The calculation was carried out by the two Krylov-subspace methods, (i) the subspace diagonalization procedure [16] and (ii) the SCOCG procedure [19], and (iii) the variational Wannier-state method [31]. In the variational Wannier-state method, the initial guesses of the wavefunctions are prepared to be the lone-pair state of $(|s\rangle + |p_z\rangle)/\sqrt{2}$ for surface states and to be the sp^3-bonding states for other (bulk) states. The three methods reproduce the energy differences satisfactorily among the (2×1), (2×2) and (4×2) surfaces, when these results are compared with those of the eigenstate calculation with the present Hamiltonian [33] and the standard *ab initio* calculation [34].

The perturbative Wannier-state method is much more limited in its applicability than the above three methods, because the unperturbed term should be prepared as a good approximation ($|\phi_i^{(WS)}\rangle \approx |\phi_i^{(WS)(0)}\rangle$ or $w_0^{(i)} \approx 1$). So far we have applied the perturbative Wannier-state method only to the bulk (sp^3-bonding) wavefunction in the diamond-structure solids without deformation or with small (elastic) deformation [11, 29, 32, 31]. Since the first-order perturbation form was used for the wavefunction $|\phi_i^{(WS)}\rangle$ in these cases, the calculated energy $\varepsilon_i^{(WS)} \equiv \langle\phi_i^{(WS)}|H|\phi_i^{(WS)}\rangle$ is correct within the second order with respect to deformation and the elastic constants are well reproduced. We should say, however, that a drastic change of wavefunction, like that in a bond-breaking process, is not reproduced by the perturbative Wannier-state method, if the bulk (sp^3-bonding) wavefunction is chosen as the unperturbed term.

Despite the limitations, the computational performance of the Wannier-state methods is faster, at best by several hundred times, than that of the Krylov-subspace method, if it is applicable. In figure 1, for example, the Wannier-state method with the perturbative procedure (WS-PT) using a single CPU is faster than the Krylov-subspace method with the subspace-diagonalization procedure (KR-SD) using 64 CPUs.

When one thinks about a guiding principle for how to choose a solver method in an application study, the above discussion suggests that the Wannier-state methods give a faster performance when the input wavefunctions are near the final solutions and, particularly, they are well localized. In other cases, the Krylov-subspace method is preferable, since the Krylov-subspace method does not require any input quantity for electronic states.

3. Theory (2) multi-solver scheme

3.1. Formulation

As another fundamental methodology for large-scale calculations, we developed a 'multi-solver' scheme [15, 31], as a hybrid or combination of two different solver methods. Its basic

idea is that the density matrix is decomposed into two parts called 'subsystems' and they are given by different solver methods. As discussed below, the multi-solver scheme will be fruitful, particularly, when the simulation system is composed of different regions, such as bulk and surface regions, and different solver methods are used in these different regions.

The mathematical foundation of the multi-solver scheme is based on the commutation relation of the density matrix,

$$[H, \rho] = 0. \tag{20}$$

When the occupied one-electron states, eigenstates or Wannier states, are classified into two groups A and B, the density matrix is decomposed into the corresponding two parts

$$\rho \equiv \rho_A + \rho_B \tag{21}$$

where

$$\rho_A \equiv \sum_i^{occ(A)} |\phi_i\rangle\langle\phi_i|, \tag{22}$$

$$\rho_B \equiv \sum_j^{occ(B)} |\phi_j\rangle\langle\phi_j| = \rho - \rho_A. \tag{23}$$

Here we call ρ_A and ρ_B 'subsystems' and the two subsystems are orthogonal

$$\rho_A \rho_B = 0, \tag{24}$$

owing to the orthogonality relation

$$\langle\phi_i|\phi_j\rangle = 0, \qquad \phi_i \in A, \phi_j \in B. \tag{25}$$

If the subsystems ρ_A and ρ_B are defined from eigenstates, a mapped Hamiltonian

$$H_{map}^{(A)} \equiv H + 2\eta_s\rho_B, \tag{26}$$

with a scalar η_s, satisfies the commutation relation

$$[H_{map}^{(A)}, \rho_A] = 0 \tag{27}$$

owing to equation (24) and

$$[H, \rho_\alpha] = 0 \quad (\alpha = A, B). \tag{28}$$

We call the scalar η_s the 'energy-shift parameter'. If ρ_B is given, the problem for obtaining ρ_A is reduced to a standard quantum mechanical problem with the well defined Hamiltonian $H_{map}^{(A)}$. In practical calculations, the energy shift parameter is chosen to be so large that the states in ρ_B do not lie in the occupied energy region of $H_{map}^{(A)}$. Note that equations (27) and (28) are satisfied, even if the subsystems ρ_A and ρ_B are constructed by eigenstates with fractional occupancy.

If the subsystems ρ_A and ρ_B are defined from Wannier states, on the other hand, equation (27) is not satisfied, because equation (28) is not satisfied. Then we redefine the mapped Hamiltonian as

$$H_{map}^{(A)} \equiv H + 2\eta_s\rho_B - H\rho_B - \rho_B H, \tag{29}$$

which satisfies equation (27) in the cases of eigenstates and Wannier states. See appendix A for proof. A simplest case is that subsystem ρ_A consists of only one Wannier state $\phi_i^{(WS)}$. In this case, the mapped Hamiltonian in equation (29) is reduced to that in equation (15), because $\rho_A \Rightarrow |\phi_i^{(WS)}\rangle\langle\phi_i^{(WS)}|$ and $\rho_B \Rightarrow \bar{\rho}_i$. In other words, the present theory gives another derivation of equation (14), the mapped equation of the Wannier state. From a practical viewpoint, the term $(H\rho_B + \rho_B H)$ in equation (29) can be ignored, when the energy shift parameter η_s is so large $(\eta_s \to +\infty)$ that the energy band of ρ_B is well separated, energetically, from that of ρ_A. If the term is ignored, the mapped Hamiltonian is reduced to the form of equation (26).
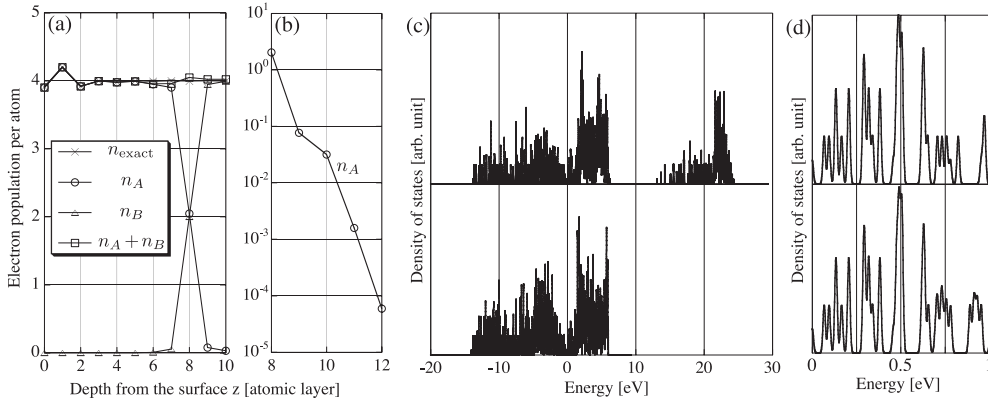
Figure 2. Example of the multi-solver scheme in a silicon slab with ideal (001) surface. (a), (b) The electron population per atom is plotted as a function of the atomic layer. The atoms at $z = 0$ correspond to the surface atoms. The calculation is carried out by the conventional eigenstate calculation (n_{exact}) and the present multi-solver scheme (n_A and n_B). (c), (d) DOS in the multi-solver scheme. Lower panel: DOS of the original Hamiltonian H. Upper panel: DOS of the mapped Hamiltonian $H_{\text{map}}^{(A)}$.

3.2. Example 1

Hereafter, the multi-solver scheme will be demonstrated. Although the formulation of the multi-solver scheme is general, we have only used, so far, the scheme with the perturbative Wannier-state method for a subsystem (ρ_B). Among these cases, subsystem ρ_B is determined in the first-order perturbation form, and then the other subsystem ρ_A is determined, through the mapped Hamiltonian $H_{\text{map}}^{(A)}$, by a different solver method ($\rho_B \Rightarrow H_{\text{map}}^{(A)} \Rightarrow \rho_A$). In other words, the present procedure does not contain a self-consistent loop ($\rho_B \Rightarrow H_{\text{map}}^{(A)} \Rightarrow \rho_A \Rightarrow H_{\text{map}}^{(B)} \Rightarrow \rho_B \cdot \cdot$). A related general discussion will be given in section 4.3.

The first example is a Si slab with ideal (001) surface, in which we use the eigenstate method for ρ_A and the perturbative Wannier-state method for ρ_B. Each atomic layer contains 64 atoms and the total number of atoms is $64 \times 16 = 1024$ in the periodic simulation cell. Since an ideal (001) surface gives an almost zero energy gap (0.025 eV), the present example is one of the severest tests for the present methodology. The z coordinate is written in the unit of atomic layers ($z = 0, 1, 2, \ldots, 15$). The surface atoms are located at $z = 0$ and have dangling-bond electrons. The atoms in the opposite surface ($z = 15$) are terminated by the bulk (sp^3-bonded) Wannier states and do not have any dangling-bond electrons. The z coordinates of bulk-bond sites can be described as half integers ($z = 0.5, 1.5, 2.5, \ldots, 14.5$). In the multi-solver scheme, subsystem ρ_B is constructed from the Wannier states whose localization (bond) centres are located deeper than the eighth atomic layer ($z = 8.5, 9.5, \ldots$). The rest of the system is assigned to the subsystem ρ_A that contains the surface states. The wavefunctions $\phi_i^{(\text{WS})}$ in ρ_B are determined by the perturbation form and, then, ρ_A is determined by diagonalizing the mapped Hamiltonian $H_{\text{map}}^{(A)}$. The energy shift parameter is chosen as $2\eta_s = 1$ au ($\approx$27.2 eV).

In figure 2(a), the electron populations of the subsystems, $n_A(z)$ and $n_B(z)$, are plotted as functions of the atomic coordinate z. The total electron population in the multi-solver scheme ($n_A + n_B$) reproduces the exact one $n_{\text{exact}}(z)$. As a remarkable result, the population at $z = 8$ is contributed by both of the subsystems, ρ_A and ρ_B, with an almost equal weight, since the Wannier states located at $z = 7.5$ and those at $z = 8.5$ belong to ρ_A and ρ_B, respectively. Figure 2(b) shows that $n_A(z)$ decays quickly at $z > 8$, because of the nature of the mapped Hamiltonian $H_{\text{map}}^{(A)}$.

So as to understand the multi-solver scheme, figures 2(c), (d) show the DOS of the original Hamiltonian and the mapped Hamiltonian $H_{\mathrm{map}}^{(A)}$. The energy origin ($\varepsilon = 0$) is chosen at the lowest unoccupied level in H. Each eigenlevel is drawn as a spike with the width of $\Delta\varepsilon = 0.02$ eV. In the DOS of the mapped Hamiltonian, the band in the occupied energy region ($\varepsilon < 0$) is that of ρ_A, while the band of ρ_B is shifted by $2\eta_s = 27.2$ eV, owing to the term of $2\eta_s\rho_B$ in $H_{\mathrm{map}}^{(A)}$, and is located at the high-energy region at 13 eV $< \varepsilon < 25$ eV. As in figure 2(d), the two DOS profiles agree excellently at the bottom of the unoccupied energy region ($0 \leqslant \varepsilon \leqslant 0.7$ eV). Here we recall that the original and mapped Hamiltonians, from their definitions, share the unoccupied eigenstates that give the density matrix of $\bar{\rho} \equiv 1 - \rho$ ($[\bar{\rho}, H] = [\bar{\rho}, H_{\mathrm{map}}^{(A)}] = 0$), and the disagreement in the present result appears only because ρ_B deviates from the exact one. The excellent agreement at the band bottom ($0 \leqslant \varepsilon \leqslant 0.7$ eV) appears since these states are contributed dominantly by surface states and are almost free from subsystem ρ_B.

3.3. Example 2

The multi-solver scheme was demonstrated in large-scale calculations. The first example is a reconstructed (001) surface of a Si slab with 10^4 atoms, which is determined with the force on atoms. The practical procedure is the same as in section 3.2, except for the point that the subsystem ρ_A is calculated by the Krylov-subspace (KR-SD) method instead of the exact diagonalization method. The result shows the correct surface reconstruction [16].

The second example is a MD simulation of a silicon nanocrystal with 4501 atoms. The multi-solver scheme is constructed from the variational Wannier-state method for ρ_A and the perturbative Wannier-state method ρ_B [31]. An external load is imposed in the [001] direction and one initial defect bond is introduced by imposing a repulsive force on an atom pair. The sample is deformed with external load, the initial defect bond and thermal motion but not fractured. The subsystems, ρ_A and ρ_B, are assigned automatically during the MD simulation, as explained below; first, all the wavefunctions are calculated by the perturbative solver method, in which the weight of the unperturbed term $w_0^{(j)}$ is defined for each wavefunction ϕ_j (see section 2.2). If the weight $w_0^{(j)}$ of a specific wavefunction is less than 95% of the averaged weight $w_0^{(\mathrm{ave})}$ ($w_0^{(j)} < 0.95\,w_0^{(\mathrm{ave})}$), the corresponding wavefunction ϕ_j is assigned to subsystem ρ_A and is determined by the variational procedure. In other words, if the perturbative procedure does not give a satisfactory accuracy, the procedure is switched automatically to the variational one. The result of the automatic assignment is shown in figure 3, in which atoms are visible only if their electron population is significantly contributed from ρ_A. As a result, subsystem ρ_A, treated by the variational procedure, appears mainly near the sample edges and in the internal region near the initial defect bond, because these regions are significantly deformed and the electronic states in these regions are fairly deviated from that in the ideal crystal.

As a technical detail of the MD simulation with the multi-solver scheme, we used a fine tuning technique for the lattice constant [31]. In calculations of an ideal silicon crystal, the equilibrium lattice constant or bond length differs by 2% between the variational and perturbative methods. The difference can cause, in principle, an artificial lattice mismatch in the multi-solver scheme, and therefore we tuned the bond length, by imposing an additional two-body classical potential on an atom pair or bond site, if the atom pair is occupied by a perturbative Wannier state. This fine tuning technique avoids the possible artificial lattice mismatch. Although the calculation results without the fine tuning (not shown) did not indicate any practical problem with our calculations of silicon, we presume that an error of 2% in lattice constant might be non-negligible in several cases. For example, the lattice constant between
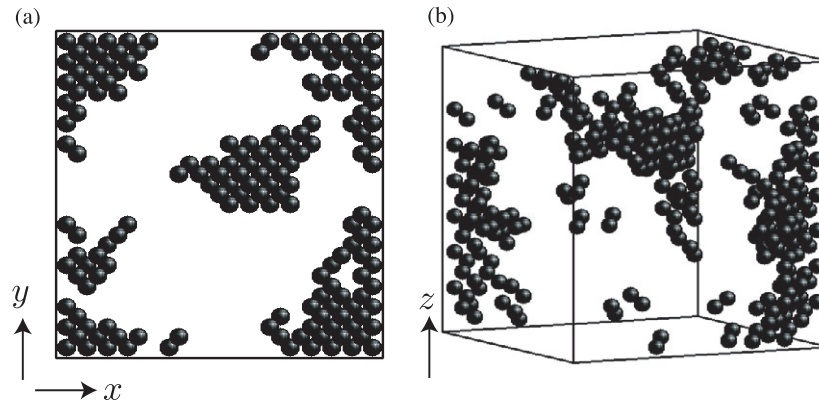
Figure 3. Multi-solver scheme with automatic assignment of subsystems (ρ_A, ρ_B). Top (a) and three-dimensional (b) views of a silicon nano-crystal with 4501 atoms. Atoms are visible only if their electron population is dominated by subsystem ρ_A. The figures are drawn in ideal crystalline geometry to guide the eye, though the actual system is deformed. The sample edges are plotted as lines to guide the eye.

Si and Ge is different by 4% and the artificial lattice mismatch by 2% might cause a problem when a Si/Ge system is calculated.

4. Applications

4.1. Liquid carbon: a metallic system

Liquid carbon was simulated with the Krylov-subspace method as a test calculation. The cubic simulation cell is used with 216 and 13 824 atoms. The density and the temperature are set to be $\rho = 2.0$ g cm^{-2} and $T = 6000$ K, respectively. The time interval between MD steps is set to be $\Delta t = 1$ fs. As technical details, the subspace dimension and the number of atoms in the real-space projection (see appendix B) are chosen to be $\nu = 30$ and $N_{PR} = 200$, respectively.

Figure 4(a) shows the resultant pair correlation (PC) function for the conventional eigenstate method with 216 atoms and for the Krylov-subspace method with 13 824 atoms. The two graphs are indistinguishable, owing to an excellent agreement. In figure 4(b), the DOS is calculated, from the Green's function, by the Krylov-subspace method with 13 824 atoms. In the DOS calculation, the controlling parameters are set into a heavier computational cost ($\nu = 300$ and $N_{RP} = 1000$), so as to reproduce the fine DOS profile. Since the present Hamiltonian includes only s and p orbitals, the resultant DOS is missing in higher energy regions. The imaginary part of the energy ($z = E + i\gamma$) is chosen at $\gamma = 0.05$ eV. The resultant DOS profile in figure 4(b) shows the correct feature of liquid carbon, as follows: a narrow π band appears, from $E = -5$ to $+5$ eV, as in nanotubes, which can be decomposed into the bonding and antibonding bands. The π bond in the liquid phase is, however, imperfect, and non-bonding (atomic) p states appear as a sharp peak near the chemical potential ($\varepsilon \approx 0.6$ eV).

Figure 4(c) shows the resultant mean square displacement (MSD) for the Krylov-subspace method (KR) and the conventional eigenstate method (EIG1, EIG2). The main figure shows a system of 216 atoms by the two methods, while the inset shows that of 13 824 atoms by the Krylov-subspace method. In the eigenstate method, the level-broadening (temperature) parameter in the Fermi–Dirac function is set to $\tau = 0.1$ eV (EIG1) and $\tau = 0.005$ au $= 0.136$ eV (EIG2), respectively, so as to show that the detailed treatment near the Fermi
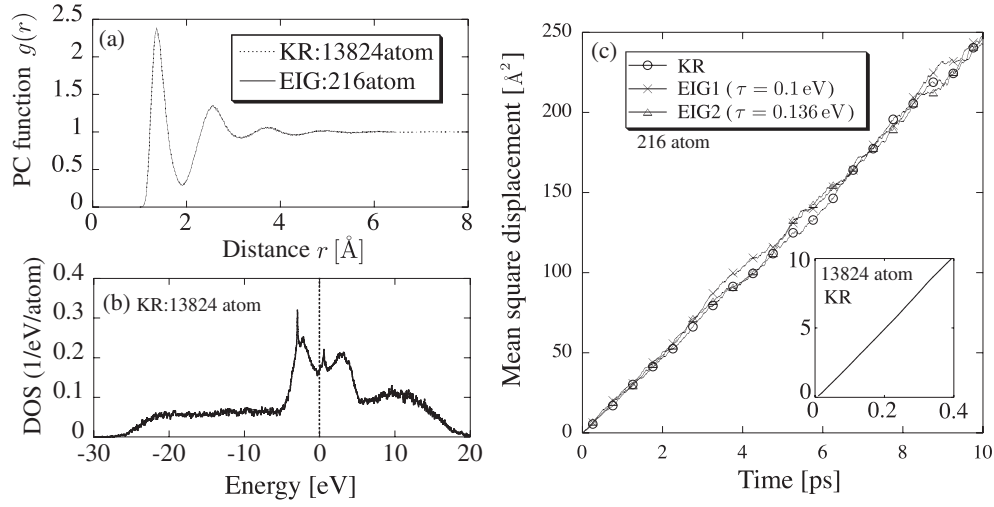
Figure 4. MD simulation of liquid carbon. (a) Pair correlation (PC) function calculated by the standard eigenstate method with 216 atoms and by the Krylov-subspace method with 13 824 atoms. In the former calculation, the function is plotted only within $r \leqslant 6.45$ Å, since the simulation cell size is smaller. (b) DOS in a snapshot with 13 824 atoms, using the Krylov-subspace method. The energy origin ($\varepsilon = 0$) is chosen at the chemical potential. (c) Mean square displacement using the Krylov-subspace method (KR) or the standard eigenstate method. In the latter method, the level-broadening parameter in the Fermi–Dirac function is set to $\tau = 0.1$ eV (EIG1) and $\tau = 0.136$ eV (EIG2). The numbers of atoms are 216 in the main figure and 13 824 in the inset, respectively.

level causes different fluctuation behaviours of the MSD. Since the difference in fluctuation behaviour is seen even among the two cases of the eigenstate method, we conclude that the Krylov-subspace method shows satisfactory agreements with the eigenstate method for PC function and diffusion constant (the gradient of the linear behaviour in the main figure of figure 4(c)).

4.2. Silicon: cleavage process

As a practical large-scale calculation, the silicon cleavage process was investigated [15, 31, 17]. The Wannier-state method is used, since it is faster than the Krylov-subspace method, when, as discussed in section 2.3, a dominant number of wavefunctions are well localized. The number of atoms in the localization region for each Wannier state ($N_A^{(i)}$) is assigned to be $N_A^{(i)} = 20$–80, which is determined by the residual norm $|\delta\phi_i^{(WS)}|^2$. The resultant density matrix has a spatial spread, in its off-site elements, over regions with hundreds of atoms. Particularly, wavefunctions near cleaved regions tend to have a large residual norm and the localization constraints on such wavefunctions are automatically relaxed to increase the number $N_A^{(i)}$. We found that such a way of controlling the accuracy for microscopic freedoms is crucial for reproducing the surface reconstruction on a cleaved surface. See [31] for details.

Figures 5(a)–(c) show a silicon cleavage process with the variational Wannier-state method. The external load is imposed on the [001] direction, as in our previous simulation [15]. The present system, unlike the previous one [15], does not contain any initial defect for a 'cleavage seed'. As a result, the cleavage starts from two points on the sample edges and two cleavage planes appear. The lower cleavage surface is shown in figures 5(d) and (e). In figure 5, a rod (atomic wavefunction) or ball (bonding wavefunction) is assigned for each wavefunction,

according to the weight distribution among atoms. The black rods are the reconstructed bonds that are not seen in the initial (crystalline) structure. A ball is assigned for an atomic (non-bonding) orbital, localized on an atom site. On the cleaved surface, an asymmetric dimer appears, as on a clean (001) surface, with a ball (lone-pair state) on the upper atom, which is shown in figure 5(g). For quantitative discussion of orbital freedoms, a parameter $f_s^{(i)}$ is defined [15], for a wavefunction ϕ_i, as

$$f_s^{(i)} \equiv \sum_I |\langle \phi_i | Is \rangle|^2, \tag{30}$$

where $|Is\rangle$ is the s orbital at the Ith atom. For example, $f_s^{(i)} = 1/4$ in an ideal sp^3 hybridized state. To visualize the orbital freedom of wavefunctions, the atomic (non-bonding) states are classified by the colour of the ball, according to the value of $f_s^{(i)}$ (see the caption of figure 5). After a bulk (sp^3) bond is broken, the corresponding wavefunction is stabilized by increasing the weight of s orbitals ($f_s^{(i)} \geqslant 0.5$), which results in the appearance of red or yellow balls on the cleaved surface.

As a remarkable result, a well defined dimer-row domain is formed by nine dimers in figure 5(e), in which the tilting freedoms of asymmetric dimers are fixed into the (2×1) configuration, although the surface energy of the (2×1) surface is higher than that of the (4×2) surface (see section 2.3). We suggest that the directional anisotropy of deformation is caused by the cleavage propagation direction, as indicated by the green arrow in figure 5(e), and gives the ordering of the tilting freedoms into the (2×1) configuration. We also calculated many other systems (not shown) in different sample geometries, which support the above suggestion.

Figure 5(h) is a larger system simulated by the multi-solver scheme, in which we use the variational and perturbative Wannier-state methods for subsystems ρ_A and ρ_B, respectively [15, 31]. The system contains 118 850 atoms and the sample dimension is $n_{110} \times n_{1\bar{1}0} \times n_{001} = 97 \times 100 \times 49$ in the unit of atomic layers, where $n_{110} = 100$ corresponds to about 20 nm. Here the subsystem ρ_A was composed of selected Wannier states near fracture regions and the rest of the electron system is defined as subsystem ρ_B. The number of Wannier states in the subsystem ρ_A is approximately 5% of the total and the computational cost by the present multi-solver scheme is nearly one-tenth of that by the single-solver calculation with the variational procedure. In figure 5(h), the electronic states in subsystem ρ_A are depicted as rods or balls and those in subsystem ρ_B are invisible. The cleavage surface in figure 5(h) contains the (001) surface but is fairly unstable with many step formations [15, 31]. See [15, 17] for the physical discussion of the instability.

4.3. General discussion on the multi-solver scheme

Finally, a general discussion is made for a practical application of the multi-solver scheme. Among the present examples, the procedure was carried out without a self-consistent loop ($\rho_B \Rightarrow H_{map}^{(A)} \Rightarrow \rho_A$), as explained at the beginning of section 3.2. The present non-selfconsistent procedure is practical, particularly, if the electron system can be decomposed into two parts that are governed by stronger and weaker binding mechanisms, respectively. In the present examples, the electronic states in the bulk part (ρ_B) are governed by a stronger binding mechanism (the sp^3 bonding) than those in surface states (ρ_A) and can be well described without any detailed information on the surface states (ρ_A). Another example of the decomposition may be a system with strong σ bonds and weak π bonds. The situation of the decomposition is a candidate for the multi-solver scheme. When the multi-solver scheme is used, the solver method for each subsystem should be chosen from the discussion of section 2.3.

We note that the multi-solver scheme with a self-consistent loop can be realized, in principle, and its practical application might be a possible future work.
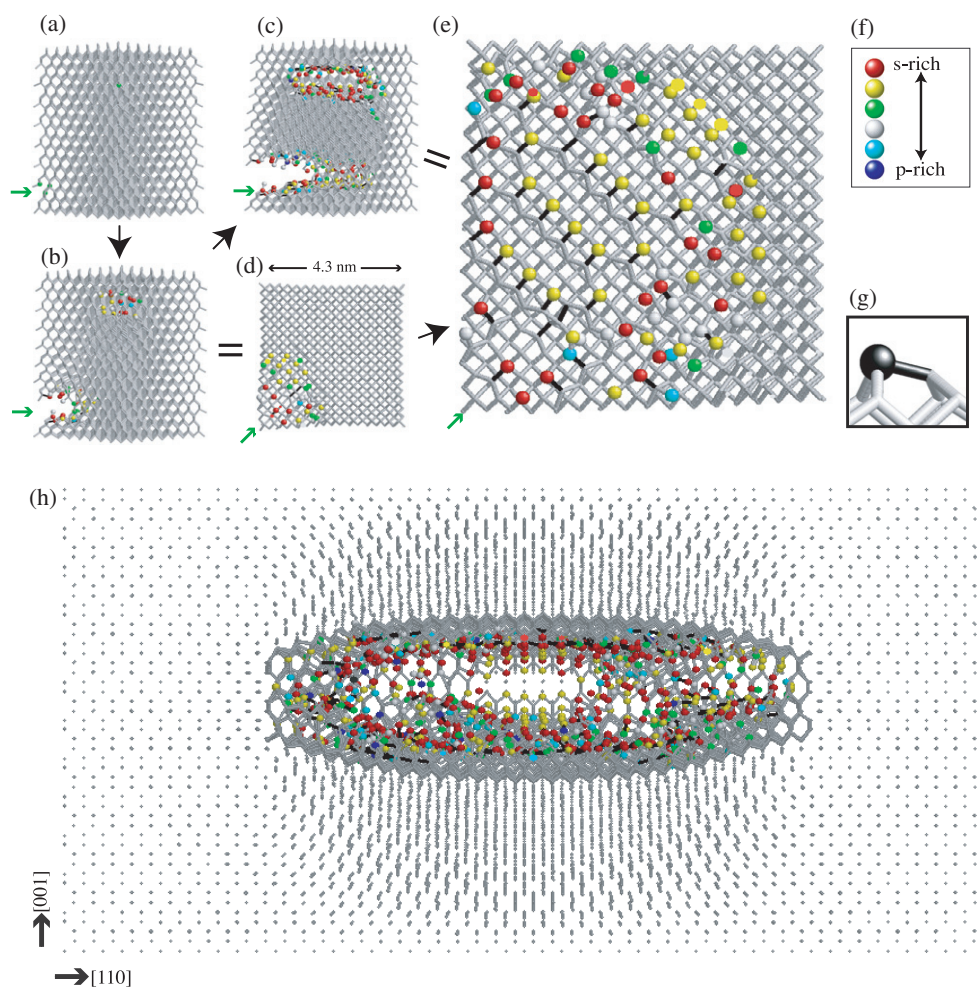
Figure 5. Cleavage process of a silicon nanocrystal under [001] external load, in which a rod indicates a bonding state and a ball indicates an atomic (non-bonding) state. (a)–(c). The 3D views of successive snapshots with the time interval of about 0.7 ps. (d), (e). Top views of the lower cleavage plane, a (001) surface, in snapshots (b) and (c), respectively. The green arrow indicates the cleavage propagation direction of the lower cleavage plane. (f) Colour samples of the atomic states (balls), which indicate the weight of s orbitals ($f_s^{(i)}$): (i) $0 \leqslant f_s^{(i)} \leqslant 0.2$ for blue, (ii) $0.2 \leqslant f_s^{(i)} \leqslant 0.3$ for cyan, (iii) $0.3 \leqslant f_s^{(i)} \leqslant 0.4$ for white, (iv) $0.4 \leqslant f_s^{(i)} \leqslant 0.5$ for green, (v) $0.5 \leqslant f_s^{(i)} \leqslant 0.6$ for yellow and (vi) $0.6 \leqslant f_s^{(i)}$ for red. (g) Example of the asymmetric dimer geometry. (h) A cleaved sample with 118 850 atoms that is calculated by the multi-solver scheme. The picture is drawn for the semi-infinite region of $y > x$. Electronic states, rods or balls, are depicted only for the subsystem ρ_A. Note that, in larger samples such as (h), the (001) cleavage mode will be fairly unstable, owing to step formations [15].

5. Concluding remarks

This paper presents fundamental theories and practical methods for large-scale electronic structure calculations, particularly for dynamical process with nm-scale or 10 nm-scale structures. First, we presented several practical solver procedures, based on the Krylov

subspace and the generalized Wannier state, so as to obtain the density matrix without calculating eigenstates. We emphasized that every method has a means of accuracy control for microscopic freedoms, by monitoring the residuals of exact equations. Second, the 'multi-solver' scheme was formulated based on the commutation relation of the density matrix, and was used for a hybrid or combined method of different solver methods. Several practical large-scale calculations were carried out in metallic and insulating cases.

These methodologies enable us to design a simulation of nanostructure processes with an optimal computational cost, in which the accuracy is controlled dynamically for microscopic (basis) freedoms and solver methods may be different among different regions. These points are essential in nanostructured systems, nm-scale or 10 nm-scale systems, because a competition between different regions, such as bulk and surface regions, is essential and is required to be reproduced in simulation. Since the above requirement is general among nanostructure processes, the present discussion is always valid, even when a different system is calculated by a different solver method from those in the present paper.

Acknowledgments

Appendix A. Proof of the fundamental equation in the multi-solver scheme

Here we prove equation (27), the fundamental equation in the multi-solver scheme, when the subsystems ρ_A, ρ_B are constructed from Wannier states in equations (22) and (23) and the mapped Hamiltonian $H_{map}^{(A)}$ is defined by equation (29). We notice that the projection operator onto the unoccupied Hilbert space, $\bar{\rho}$, is defined as

$$\bar{\rho} \equiv 1 - \rho = 1 - \rho_A - \rho_B \tag{A.1}$$

and satisfies

$$H\bar{\rho} = \bar{\rho}H. \tag{A.2}$$

Equation (27) is satisfied as follows:

$$
\begin{aligned}
\left[H_{map}^{(A)}, \rho_A\right] &= [H, \rho_A] + 2\eta_s[\rho_B, \rho_A] - [H\rho_B + \rho_B H, \rho_A] \\
&= (H\rho_A - \rho_A H) + 0 - (\rho_B H\rho_A - \rho_A H\rho_B) \\
&= (1 - \rho_B)H\rho_A - \rho_A H(1 - \rho_B) \\
&= (\bar{\rho} + \rho_A)H\rho_A - \rho_A H(\bar{\rho} + \rho_A) \\
&= \bar{\rho}H\rho_A - \rho_A H\bar{\rho} \\
&= H\bar{\rho}\rho_A - \rho_A\bar{\rho}H = 0,
\end{aligned}
\tag{A.3}
$$

where the second equality is obtained by equations (24) and the fourth and sixth equalities are obtained by equation (A.1) and equation (A.2), respectively. The last equality is obtained by the orthogonality relation of $\bar{\rho}\rho_A = \rho_A\bar{\rho} = 0$.
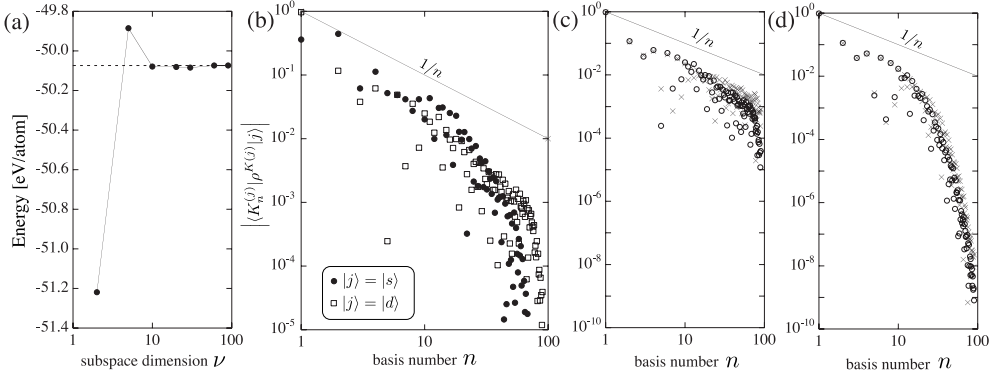
Figure B.1. Krylov-subspace method for an fcc Cu system with 10 800 atoms. (a) The convergence behaviour of the band structure energy as a function of the subspace dimension ν ($\nu = 2, 5, 10, 20, 30, 60$ and 90). A reference value calculated by the standard eigenstate method is plotted as a dashed line. (b) The decay behaviour of the density matrix $\langle K_n^{(j)} | \rho^{K(j)} | j \rangle$, as the function of the basis number (n). The subspace dimension is set to be $\nu = 90$ and the temperature (level-broadening) parameter is set to be $\tau = 0.1$ eV. The circle and square indicate the values with the starting bases of the s and d (e_g) orbitals ($|j\rangle = |s\rangle$, $|e_g\rangle$), respectively. (c), (d) Decay behaviour of the density matrix $\langle K_n^{(j)} | \rho^{K(j)} | j \rangle$ with respect to the basis number of the Krylov subspace (n). The circles indicate the result of the 10 800-atom system with the real-space projection and the crosses indicate the result of the 876-atom system without the real-space projection. The starting basis ($|j\rangle$) is chosen to be a d (e_g) orbital. The temperature (level-broadening) parameter is set to be $\tau = 0.1$ eV in (c) and $\tau = 0.5$ eV in (d).

Appendix B. Technical details and numerical aspects of the Krylov-subspace method

Here we discuss several technical details of the Krylov-subspace method and demonstrate how the method works, particularly in metals. As a demonstration, an fcc Cu system was calculated with a periodic simulation cell of 10 800 atoms. The temperature (level-broadening) parameter in the Fermi–Dirac function is set to be $\tau = 0.1$ eV. As a practical technique, a real-space projection technique is introduced; the Krylov subspace is generated by a Hamiltonian projected in real space, $H^{(j)} \equiv P^{(j)} H P^{(j)}$, instead of the original one H, where the projection operator $P^{(j)}$ projects a function onto the spherical region whose centre is located at the atomic position of the jth atomic basis. The resultant Krylov subspace is the same as the original one ($\mathcal{K}_n(H, |j\rangle) = \mathcal{K}_n(H^{(j)}, |j\rangle)$), while the bases lie within the projection region ($(H^{(j)})^n |j\rangle = H^n |j\rangle$). Since the procedure of constructing the Krylov subspace $\mathcal{K}_\nu(H^{(j)}, |j\rangle)$ is independent among the starting bases (j), all the procedures and the quantities are well defined with the real-space projection technique. The projection radius is determined for each starting basis $|j\rangle$, so that a given number of atoms, N_{RP}, should be contained inside the radius. The present calculation with 10 800 atoms was carried out using the projection technique with $N_{RP} = 381$. The calculation without the projection technique was also carried out in a smaller (876-atom) system, which is discussed below.

In figure B.1(a), the convergence behaviour of the calculated band structure energy is shown as a function of the subspace dimension, in which a reference value is also calculated by standard eigenstate calculation with the standard Brillouin-zone integration. The deviation from the reference value is about 0.01 eV per atom for $\nu = 10, 20$ and 30 and less than 1 meV per atom for $\nu = 60$ and 90. Since the density matrix ρ_{ij} is calculated in the form of equation (8), its representation within the Krylov subspace $\langle K_n^{(j)} | \rho^{K(j)} | j \rangle (= \langle K_n^{(j)} | \rho^{K(j)} | K_1^{(j)} \rangle)$ is plotted in figure B.1(b), where the starting bases $|j\rangle$ are set to be s and d (e_g) orbitals, as examples.

In figure B.1(b), we observe a $1/n$ or faster decay, and this observation is also seen with the other starting bases (p and t_{2g} orbitals). The decay behaviour of figure B.1(b) is explained by a general mathematical analysis of the Lanczos procedure [16], in which a $1/n$ decay should appear with the zero-temperature formulation ($\tau = 0$) and a faster decay should appear with a finite temperature formulation ($\tau \neq 0$). The quantity $\langle i|K_n^{(j)}\rangle$, on the other hand, also decays as $1/n$ or faster (not shown), since the (normalized) vector $|K_n^{(j)}\rangle$ has a spatial spread within the nth hopping range from the starting basis ($|K_n^{(j)}\rangle \in \mathcal{K}_n(H,|j\rangle)$). Consequently, their product ($\langle i|K_n^{(j)}\rangle\langle K_n^{(j)}|\rho^{K(j)}|j\rangle$) decays as $1/n^2$ or faster, which validates the fast convergence in the summation of equation (8).

We should emphasize that the decay behaviour in figure B.1(b) comes from a general property of the Lanczos procedure, as discussed above, *not* from the projection technique. The above statement is confirmed numerically in figures B.1(c), (d), in which fcc Cu systems were calculated with or without the real-space projection and the resultant decay behaviour is affected significantly by the temperature (level-broadening) parameter τ, but not by the projection technique.

References

[1] Car R and Parrinello M 1985 *Phys. Rev. Lett.* **55** 2471
[2] Kohn W 1996 *Phys. Rev. Lett.* **76** 3168
[3] Galli G 2000 *Phys. Status Solidi* b **217** 231
[4] Wu S Y and Jayamthi C S 2002 *Phys. Rep.* **358** 1
[5] Mauri F, Galli G and Car R 1993 *Phys. Rev.* B **47** 9973
[6] Li X-P, Nunes R W and Vanderbilt D 1993 *Phys. Rev.* B **47** 10891
[7] Ordejón P, Drabold D A, Grumbach M P and Martin R 1993 *Phys. Rev.* B **48** 14646
[8] Goedecker S and Colombo L 1994 *Phys. Rev. Lett.* **73** 122
[9] Hoshi T and Fujiwara T 1997 *J. Phys. Soc. Japan* **66** 3710
[10] Roche S and Mayou D 1997 *Phys. Rev. Lett.* **79** 2518
[11] Hoshi T and Fujiwara T 2000 *J. Phys. Soc. Japan* **69** 3773
[12] Ozaki T and Terakura K 2001 *Phys. Rev.* B **64** 195126
[13] Soler J M, Artacho E, Gale J D, García A, Junquera J, Ordejón P and Sánchez-Portal D 2002 *J. Phys.: Condens. Matter* **14** 2745
[14] Bowler D R, Miyazaki T and Gillan M J 2002 *J. Phys.: Condens. Matter* **14** 2781
[15] Hoshi T and Fujiwara T 2003 *J. Phys. Soc. Japan* **72** 2429
[16] Takayama R, Hoshi T and Fujiwara T 2004 *J. Phys. Soc. Japan* **73** 1519
[17] Hoshi T, Iguchi Y and Fujiwara T 2005 *Phys. Rev.* B **72** 075323
[18] Skylaris C-K, Haynes P D, Mostofi A A and Payne M C 2005 *J. Chem. Phys.* **122** 084119
[19] Takayama R, Hoshi T, Sogabe T, Zhang S-L and Fujiwara T 2006 *Phys. Rev.* B **73** 165108
[20] Hoshi T, Takayama R, Iguchi Y and Fujiwara T 2006 *Physica* B **376/377** 975
[21] Andersen O K and Jepsen O 1984 *Phys. Rev. Lett.* **53** 2571
[22] Xu C H, Wang C Z, Chan C T and Ho K M 1992 *J. Phys.: Condens. Matter* **4** 6047
[23] Kwon I, Biswas R, Wang C Z, Ho K M and Soukoulis C M 1994 *Phys. Rev.* B **49** 7242
[24] van der Vorst H A 2003 *Iterative Krylov Methods for Large Linear Systems* (Cambridge: Cambridge University Press)
[25] Frommer A 2003 *Computing* **70** 87
[26] Kohn W 1973 *Phys. Rev.* B **7** 4388
[27] Kohn W 1993 *Chem. Phys. Lett.* **208** 167
[28] Marzari N and Vanderbilt D 1997 *Phys. Rev.* B **56** 12847
[29] Hoshi T and Fujiwara T 2001 *Surf. Sci.* **493** 659
[30] Andersen O K, Saha-Dasgupta T and Ezhov S 2003 *Bull. Mater. Sci.* **26** 19
[31] Hoshi T 2003 *Docter Thesis* School of Engineering, University of Tokyo, Tokyo
[32] Geshi M, Hoshi T and Fujiwara T 2003 *J. Phys. Soc. Japan* **72** 2880
[33] Fu C C, Weissman M and Saúl A 2001 *Surf. Sci.* **494** 119
[34] Ramstad R, Brocks G and Kelly P J 1995 *Phys. Rev.* B **51** 14504